Acta Mechanica Sinica (2014) 30(6):819–827
DOI 10.1007/s10409-014-0095-9

RESEARCH PAPER

Effects of wing deformation on aerodynamic performance of a revolving insect wing

Ryusuke Noda · Toshiyuki Nakata · Hao Liu

Received: 4 September 2014 / Revised: 22 November 2014 / Accepted: 18 December 2014

Abstract Flexible wings of insects and bio-inspired micro air vehicles generally deform remarkably during flapping flight owing to aerodynamic and inertial forces, which is of highly nonlinear fluid-structure interaction (FSI) problems. To elucidate the novel mechanisms associated with flexible wing aerodynamics in the low Reynolds number regime, we have built up a FSI model of a hawkmoth wing undergoing revolving and made an investigation on the effects of flexible wing deformation on aerodynamic performance of the revolving wing model. To take into account the characteristics of flapping wing kinematics we designed a kinematic model for the revolving wing in two-fold: acceleration and steady rotation, which are based on hovering wing kinematics of hawkmoth, *Manduca sexta*. Our results show that both aerodynamic and inertial forces demonstrate a pronounced increase during acceleration phase, which results in a significant wing deformation. While the aerodynamic force turns to reduce after the wing acceleration terminates due to the burst and detachment of leading-edge vortices (LEVs), the dynamic wing deformation seem to delay the burst of LEVs and hence to augment the aerodynamic force during and even after the acceleration. During the phase of steady rotation, the flexible wing model generates more vertical force at higher angles of attack (40°–60°) but less horizontal force than those of a rigid wing model. This is because the wing twist in spanwise owing to aerodynamic forces results in a reduction in the effective angle of attack at wing tip, which leads to enhancing the aerodynamics performance by increasing the vertical force while reducing the horizontal force. Moreover, our results point out the importance of the fluid-structure interaction in evaluating flexible wing aerodynamics: the wing deformation does play a significant role in enhancing the aerodynamic performances but works differently during acceleration and steady rotation, which is mainly induced by inertial force in acceleration but by aerodynamic forces in steady rotation.

Keywords Insect flight · Flexible wing · Revolving wing · Fluid-structure interaction

1 Introduction

Flexible wings of insects and flapping-winged micro air vehicles (MAV) are generally shaped thin and flat with light structures. Both bioflyers and bio-inspired flapping MAVs flap their wings with high flapping frequencies to stay airborne, and within each beat cycle flapping wings repeates acceleration and deceleration and normally are deformed significantly due to inertial and aerodynamic forces. This is of highly nonlinear fluid-structure interaction (FSI) problems. While many studies have been undertaken [1, 2, 4–6] till now relating flexible wing aerodynamics but mostly focused on flapping wing aeordynamics with prescribed wing deformations, the FSI-induced wing deformation and its effect on flapping flexible wing aerodynamics and energetics are still a main subject with very limited studies done because of the complexity of nonlinear interactions between flapping wing aerodynamics and structural dynamics [3].

As a simplified model for flapping wings, aerodynamics of revolving wing models have also been a subject recently, which are conducted either by means of dynami-

---

R. Noda · H. Liu (✉)
Graduate School of Engineering,
Chiba University, 1-33, Yayoi-cho, Inage-ku, Chiba, Japan
Shanghai Jiao Tong University and Chiba University
International Cooperative Research Center (SJTU-CU ICRC),
Shanghai, China
e-mail: hliu@faculty.chiba-u.jp

T. Nakata
Structure and Motion Laboratory,
The Royal Veterinary College,
University of London, Hawkshead Lane,
North Mymms, Hatfield, AL9 7TA, United Kingdom

cally scaled mechanical robots [7–10] or by computational fluid dynamic models [11–13] in the low Reynolds number regime. These models present the general aerodynamic performance of a flapping wing by force coefficients that can be estimated with blade element models, and the effects of wing planform shape, twist and camber on the revolving wing aerodynamics can be further investigated in a separated way [7, 11–13]. Such revolving wing models with a simplified kinematics may be an essential model for an integrated understanding of the essence of flapping wing aerodynamics in a manner of separating some novel mechanisms such as the LEV and other force enhancement mechanisms from the complexity of flapping wing systems.

In this study, we aim at establishing a FSI model of a revolving insect wing to tackle the nonlinear FSI problem associated with flexible wing aerodynamics at low Reynolds numbers. Follow our previous computational FSI analysis [3] of flexible flapping wing aerodynamics that utilized a realistic morphological and structural model of hawkmoth wing, we constructed our revolving wing kinematics on the basis of the realistic wing kinematics of a hovering hawkmoth with a Reynolds number and the characteristics of acceleration identical to those of the hovering hawkmoth [3]. The kinematic model for the revolving wing is designed in two-fold: acceleration and steady rotation, in which the wing is accelerated around a pivot at wing base from rest and continues steady rotation after reaching the mean angular velocity of a hovering hawkmoth. The wing deformation, and the vertical and horizontal forces of the flexible revolving wing are simulated and compared with those of a rigid revolving wing. We further give an extended discussion on wing aerodynamics and energetics during the phases of acceleration and steady rotation and its correlations with wing deformations as well as its discrepancy compared with the rigid flapping wing.

2 Method

2.1 Morphological wing model and revolving wing kinematics

In this study, we use a hawkmoth wing model that was originally developed by Aono and Liu [14] on the basis of the two-dimensional digitized image of hawkmoth, *Agrius vonvolvuli*. The wing length R and mean chord length c_m are 5.05 and 1.83 cm, respectively. Figure 1 shows the hawkmoth wing model and the coordinate system used in this study.

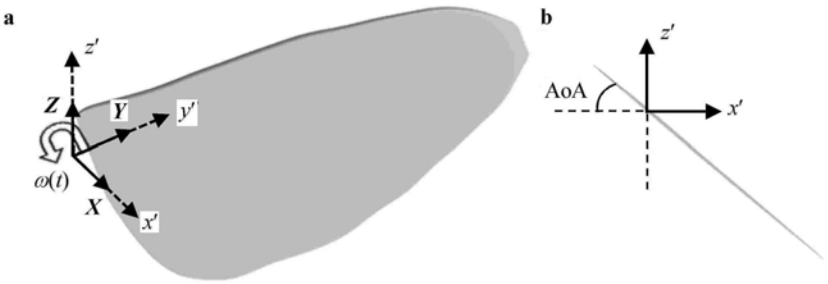

Fig. 1 **a** A hawkmoth wing model with a global coordinate system (X, Y, Z) and a wing-fixed coordinate system (x', y', z'); **b** Definition of angle of attack (AoA) at wing base

The inertial force as well as aerodynamic force can have significant effects on wing deformations [15]. Therefore, the kinematic model of a revolving wing is constructed by simplifying the realistic wing kinematic of a hovering hawkmoth so that the Reynolds number and acceleration of the wing can be same with that of the hawkmoth's wing in hovering. The angular velocity of revolving wing ω is defined as follows

$$\omega(t) = \begin{cases} \Omega \cos\left[\dfrac{1}{2}\left(1 + \dfrac{t}{T_\mathrm{accel}}\right)\pi\right], & t < T_\mathrm{accel}, \\ \Omega, & T_\mathrm{accel} \geqslant t, \end{cases} \tag{1}$$

where Ω is rotational angular velocity, t is dimensionless time and T_accel is the time when the wing terminates its acceleration and starts steady rotation. In this study, T_accel is defined by using the wing kinematics of a hovering hawkmoth, *Manduca sexta* [14, 16]. As shown in Fig. 2, the wing tip velocity reaches its maxima when the flapping-wing tip acceleration of the hovering hawkmoth becomes zero at about 0.15 flapping period, which is identical to a dimensionless time of approximately 1.64 after stroke reversal. We utilize this value as T_accel in Eq. (1). The rotational velocity Ω in Eq. (1) is calculated to be 104.41 rad/s. The time-history of the angular velocity ω during the acceleration phase is also plotted in Fig. 2. The wing model keeps rotation up to three revolving cycles after T_accel during the phase of steady rotation. The Reynolds number Re is defined as $Re = U_\mathrm{ref} c_\mathrm{m}/\nu$, where U_ref is reference velocity and ν is the kinematic viscosity of air (1.5×10^{-5} m^2/s). The mean chord length c_m is used as the reference length, and the U_ref is defined as ΩR, the wing tip velocity of the rigid wing in steady rotation. Hence, Re is calculated to be approximately 6 400.

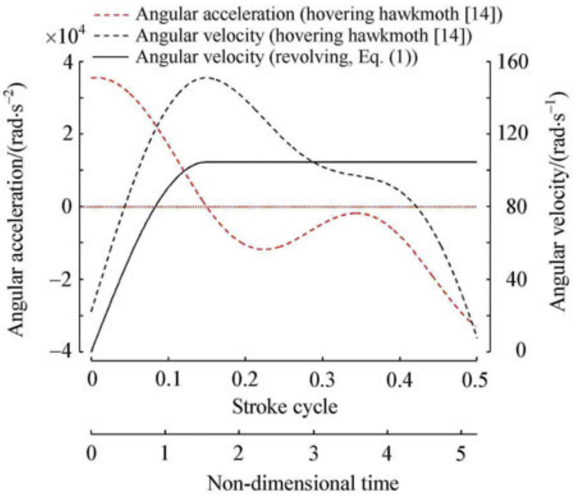

Fig. 2 Time courses of angular velocities and accelerations

2.2 Fluid-structure interaction (FSI) model

Analysis of the flexible revolving wing aerodynamics was conducted with an *in-house* fluid-structure interaction (FSI) solver developed by Nakata and Liu [17]. This FSI solver consists of a computational fluid dynamics (CFD) solver based on a fortified Navier–Stokes solver [18, 19] and a computational structural dynamic (CSD) solver [17] based on the finite element method specialized for thin structure such as insect wing. The CFD and CSD solvers are coupled in a manner of loose coupling. Note that the hawkmoth body model, which was used as a global grid in previous studies, is replaced with a sufficient small cylinder, which has been confirmed having negligible influence on the revolving wing aerodynamics. Both CFD grids and CSD meshes used in this study are illustrated in Fig. 3. More details including about the CFD and CSD models can be found in Nakata and Liu [17].

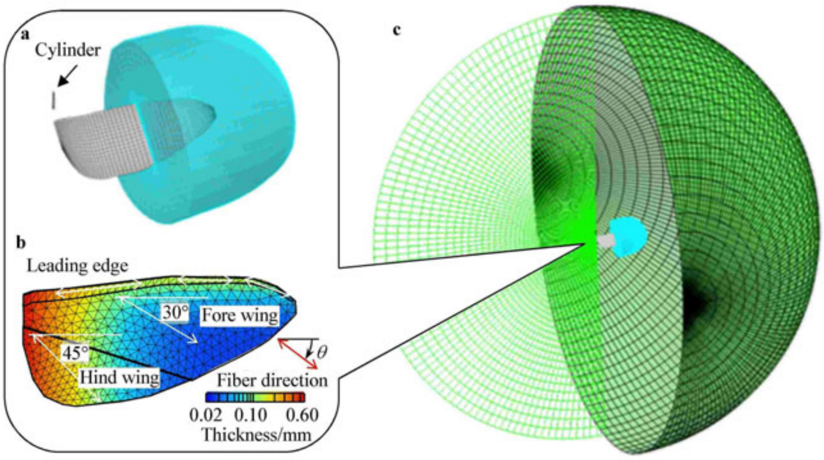

Fig. 3 Grid systems. **a** Local grid for CFD analysis; **b** A FEM mesh model of a hawkmoth wing; **c** Global grids for CFD analysis. Note that a local tiny cylinder grid is set merely for generating global grids and its influence is negligible

2.3 Computational fluid dynamic solver

A general formulation of the multi-blocked, overset grid, fortified solutions to the Navier–Stokes equations is performed in the global system (X, Y, Z) as depicted in Figs. 3a and 3b. The algorithm employed here is based on a single Navier–Stokes solver as in Liu and Kawachi [18] but is extended to a multi-blocked, overset-grid system by means of the fortified solution algorithm [19]. The governing equations are the three-dimensional, incompressible, unsteady Navier–Stokes equations written in strong conservation form for mass and momentum. The artificial compressibility method is used by adding a pseudo time derivative of pressure to the equation of continuity. For an arbitrary deformable control volume $V(t)$, the non-dimensionalized governing equations are

$$\int_{V(t)} \left(\frac{\partial \boldsymbol{Q}}{\partial t} + \frac{\partial \boldsymbol{q}}{\partial \tau} \right) \mathrm{d}V + \int_{V(t)} \left(\frac{\partial \boldsymbol{F}}{\partial x} + \frac{\partial \boldsymbol{G}}{\partial y} + \frac{\partial \boldsymbol{H}}{\partial z} + \frac{\partial \boldsymbol{F}_v}{\partial x} + \frac{\partial \boldsymbol{G}_v}{\partial y} + \frac{\partial \boldsymbol{H}_v}{\partial z} \right) \mathrm{d}V, \qquad (2)$$

where

$$\boldsymbol{Q} = \begin{bmatrix} u \\ v \\ w \\ 0 \end{bmatrix}, \qquad \boldsymbol{q} = \begin{bmatrix} u \\ v \\ w \\ p \end{bmatrix},$$

$$\boldsymbol{F} = \begin{bmatrix} u^2 + p \\ uv \\ uw \\ \lambda u \end{bmatrix}, \qquad \boldsymbol{G} = \begin{bmatrix} vu \\ v^2 + p \\ vw \\ \lambda v \end{bmatrix},$$

$$\boldsymbol{H} = \begin{bmatrix} wu \\ wv \\ w^2 + p \\ \lambda w \end{bmatrix}, \qquad \boldsymbol{F}_v = -\frac{1}{Re}\begin{bmatrix} 2u_x \\ u_y + v_x \\ u_z + w_x \\ 0 \end{bmatrix},$$

$$\boldsymbol{G}_v = -\frac{1}{Re}\begin{bmatrix} v_{x+}u_y \\ 2v_y \\ v_z + w_y \\ 0 \end{bmatrix}, \quad \boldsymbol{H}_v = -\frac{1}{Re}\begin{bmatrix} w_{x+}u_z \\ w_{y+}v_z \\ 2w_z \\ 0 \end{bmatrix}.$$

In the preceding equations, λ is the pseudo-compressibility coefficient; p is pressure; u, v, and w are velocity components in Cartesian coordinate system X, Y, and Z; t denotes physical time while τ is pseudo time; and Re is the Reynolds number. Note that the term $\boldsymbol{q}$ associated with the pseudo time is designed for an inner-iteration at each physical time step, and will vanish when the divergence of velocity is driven to zero so as to satisfy the equation of continuity. The pseudo-compressibility coefficient λ is set to be 1.0 for all the cases.

The fortified Navier–Stokes solution algorithm is achieved by adding forcing terms to the Navier–Stokes equations; by introducing the generalized Reynolds transport theorem and by employing the Gauss integration theorem, an integrated form of Eq. (4) in general curvilinear coordinate system is obtained as

$$\int_{V(t)} \frac{\partial \boldsymbol{q}}{\partial \tau}\mathrm{d}V + \frac{\partial}{\partial t}\int_{V(t)} \boldsymbol{Q}\mathrm{d}V + \oint_{S(t)} (\boldsymbol{f} - \boldsymbol{Q}\boldsymbol{u}_g)\cdot \boldsymbol{n}\mathrm{d}S$$
$$= \sigma(\boldsymbol{q}_\mathrm{f} - \boldsymbol{q}), \tag{3}$$

where $\boldsymbol{f} = (\boldsymbol{F} + \boldsymbol{F}_v, \boldsymbol{G} + \boldsymbol{G}_v, \boldsymbol{H} + \boldsymbol{H}_v)$; $S(t)$ denotes the surface of the control volume; $\boldsymbol{n} = (n_x, n_y, n_z)$ are components of the unit outward normal vector corresponding to all the faces of the polyhedron cell; $\boldsymbol{U}_g$ is the local velocity of the moving cell surface. The switching parameter σ is set to be sufficiently large, compared to all the other terms in the region, and where the solution $\boldsymbol{q}_\mathrm{f}$ is available by the subset equations, and zero outside the region. For $\sigma \gg 1$, the added source term simply forces $\boldsymbol{q} = \boldsymbol{q}_\mathrm{f}$; otherwise it blends $\boldsymbol{q}$ with $\boldsymbol{q}_\mathrm{f}$. When $\sigma = 0$, the equations go back to the ordinary Navier–Stokes equations.

The solutions to the multi-blocked, overset grid Navier–Stokes equations require specific boundary conditions at the overlapping zone stencils among grids, at the solid walls of a revolving wing and a cylinder as well as at the far field outside boundary as shown in Fig. 3a. For two single grid blocks, we solve the fortified Navier–Stokes equations two times at each time step [19]. For the holes inside the grid and the outermost two grid points, the $\boldsymbol{q}_\mathrm{f}$ are specified there by $\boldsymbol{q}$ of overlapping zones with other single grid at previous time step. Inside the computational domain except the holes and the single grid boundary $\boldsymbol{q}$ are equal to $\boldsymbol{q}_\mathrm{f}$ by setting $\sigma = 0$.

When the Navier–Stokes equations are solved for each block, the aerodynamic forces $\boldsymbol{F}_\mathrm{aero} = (F_{\mathrm{a}x}, F_{\mathrm{a}y}, F_{\mathrm{a}z})$ exerted on the wing is evaluated by a sum of aerodynamic forces in the global coordinate system. In this study, the vertical and horizontal forces coefficients C_v and C_h on a revolving wing are defined in the same way as in Ref. [7] such as

$$C_\mathrm{v} = \frac{F_{\mathrm{a}z}}{\rho S_2 \Omega^2}, \tag{4}$$

$$C_\mathrm{h} = \frac{T_{\mathrm{a}z}}{\rho S_3 \Omega^2}, \tag{5}$$

where $F_{\mathrm{a}z}$ is the aerodynamic vertical force on a single wing, $T_{\mathrm{a}z}$ is the torque about the rotational axis, S_2 and S_3 are the second and third moments of area for a single wing [20], respectively.

2.4 Computational structural dynamic solver

In order to simulate dynamics and large deformations of insect wings due to inertial and aerodynamic forces under revolving motion, a finite element method (FEM)-based structural dynamic solver is employed [17]. To model a thin structure like insect wing, we employ a triangular shell element termed AT/DKT with a very thin and anisotropic structure, which combines an Allman membrane triangular (AT) element with a discrete Kirchhoff triangular (DKT) element [21]. The element is hereby further utilized to study nonlinear dynamic response by introducing an updated Lagrangian (UL) formulation [22, 23]. The virtual work principle for a single element at time $t + \Delta t$ can be expressed as

$$\int \delta\boldsymbol{\varepsilon}^\mathrm{T}\boldsymbol{s}\mathrm{d}V + \int \rho_\mathrm{s}\delta\boldsymbol{R}^\mathrm{T}\ddot{\boldsymbol{R}}\mathrm{d}V = \delta W_\mathrm{e}, \tag{6}$$

where ρ_s is the density of a wing; $\boldsymbol{R}$ is the position in reference to the origin of the global coordinate system at time $t+\Delta t$; $\boldsymbol{s}$ and $\boldsymbol{\varepsilon}$ are the vectors of second Piola–Kirchhoff stress and incremental Green–Lagrange strain form the configuration at time t to the configuration at time $t + \Delta t$, respectively; δW_e is the virtual work done by external forces $\boldsymbol{F}$ such as fluid force. By using the nodal displacement due to elastic deformation in reference to the wing base-fixed frame $\boldsymbol{u}_\mathrm{s}$ and shape functions of AT/DKT elements [21], the integrals of Eq. (6), representing the virtual work due to internal and inertial forces in an element, can be given by

$$\int \rho_\mathrm{s}\delta\boldsymbol{R}^\mathrm{T}\ddot{\boldsymbol{R}}\mathrm{d}V = \delta u^\mathrm{T}(\boldsymbol{M}\ddot{\boldsymbol{u}}_\mathrm{s} + \boldsymbol{h}), \tag{7}$$

$$\int \delta\boldsymbol{\varepsilon}^\mathrm{T}\boldsymbol{s}\mathrm{d}V = \delta u^\mathrm{T}(\boldsymbol{K}\boldsymbol{u}_\mathrm{s} + \boldsymbol{f}_i), \tag{8}$$

where $\boldsymbol{K}$ is the tangent stiffness matrix; $\boldsymbol{M}$ is the consistent mass matrix; $\boldsymbol{f}_i$ is the internal force vector; $\boldsymbol{h}$ represents the inertial forces by prescribed flapping motion. The equilibrium equation given by substituting Eqs. (7) and (8) into Eq. (6) is assembled to form the global incremental equilibrium equation. The nonlinear equation of motion is solved by using the Newton–Raphson method combining with Wilson θ integration scheme, which may be expressed as

$$\boldsymbol{K}^{(i-1)}\Delta\boldsymbol{u}_{\mathrm{s}}^{(i)} = \boldsymbol{F} - \boldsymbol{f}_i^{(i-1)} - \boldsymbol{M}\ddot{\boldsymbol{u}}_{\mathrm{s}}^{(i-1)} - \boldsymbol{h}_{\mathrm{e}}, \tag{9}$$

where $\boldsymbol{u}_{\mathrm{s}}^{(i)} = \boldsymbol{u}_{\mathrm{s}}^{(i-1)} + \Delta\boldsymbol{u}_{\mathrm{s}}^{(i)}$. The superscripts of $\boldsymbol{K}^{(i-1)}$ and $\boldsymbol{f}_i^{(i-1)}$ denote the previous time of $i-1$ when $\boldsymbol{u}_{\mathrm{s}}^{(i-1)}$ [22].

3 Results and discussion

3.1 Force generation in rigid and flexible revolving wings

Figures 4a and 4b show time courses of vertical and horizontal force coefficients plotted against angles of wing revolution. Non-dimensional time is depicted on the horizontal axis for reference. It is seen that the aerodynamic forces of both rigid and flexible wings show a rapid increase immediately after the onset of wing revolution, which is more obvious at higher angles of attack (40°–60°) due to the added mass. Note that the aerodynamic forces are apparently enlarged in the flexible wing during the acceleration phase (An extensive discussion on discrepancy between rigid and flexible wing will be given in Sect. 3.3). The aerodynamic forces are relatively stable after the unsteady (acceleration) phase (0°–180°) but turn to decrease gradually after 360° when the wing encounters and passes through the downwash generated during the first cycle. A bigger drop in both vertical and horizontal forces is then observed at higher angles of attack (40°–60°). As postulated by Usherwood and Ellington [7] a full development of the vortex-structured wake with its associated radial inflow over the wing can shift the position of vortex breakdown inwards under steady rotational conditions at higher angles of attack and hence lead to a reduction in vertical force. At lower angles of attack (10°–20°), both vertical and horizontal forces converge comparatively faster and then keep almost constant without fluctuations till 1 080°. Such decreasing in aerodynamic forces are continuously observed from 360° to 720°, but then the aerodynamic forces turn out to be unstable fluctuating largely at larger angles of arrack even though the wake is fully developed after the second cycle. Such time-varying feature of aerodynamic forces against angles of attack is also observed in experimental studies [7, 10]. For the sake of discussion, we have defined the interval from 0° to 180° as unsteady (acceleration) phase, and the interval from 720° to 1 080° as steady (rotation) phase, and the averaged forces during each interval will be used for the following discussions.

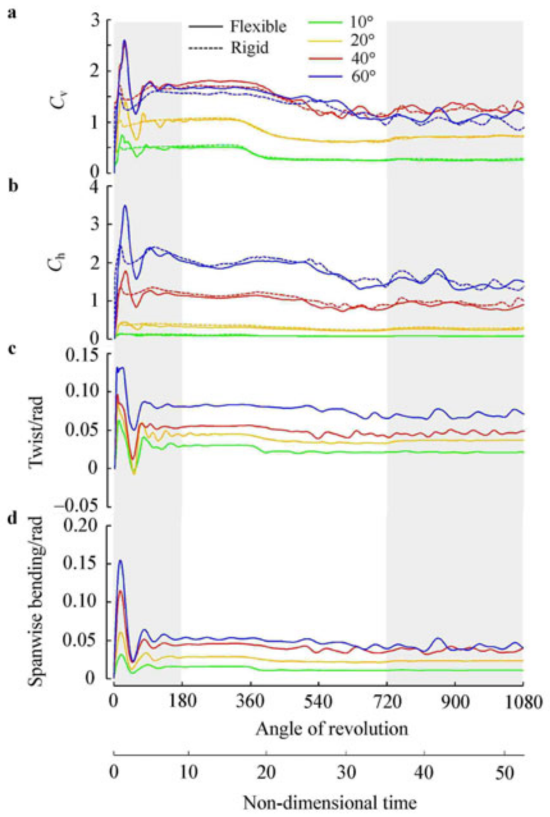

Fig. 4 Time courses of **a** vertical and **b** horizontal force coefficients generated by revolving flexible and rigid wings, and **c** twist, **d** spanwise bending of a flexible revolving wing. Shaded area corresponds to unsteady (0°–180°) and steady (720°–1 080°) phases

3.2 Wing deformations in flexible revolving wing

Twist and spanwise bending at 0.8R are further plotted against angle of wing revolution as illustrated in Figs. 4c and 4d. Note that the twist angle θ_{tw} and the spanwise bending angle θ_{b} are defined in a wing base-fixed coordinate system as depicted in Fig. 5. Both the twist and spanwise bending are observed increasing with increasing angle of attack throughout most of the period of the simulation. During the acceleration phase, the wing changes its shape rapidly and the wing deformation is maximized around a phase of 20°, where the largest twist and spanwise bending are approximately 7.2° and 8.6°, respectively. Such large wing deformation is thought due to the large inertial forces [15] as well

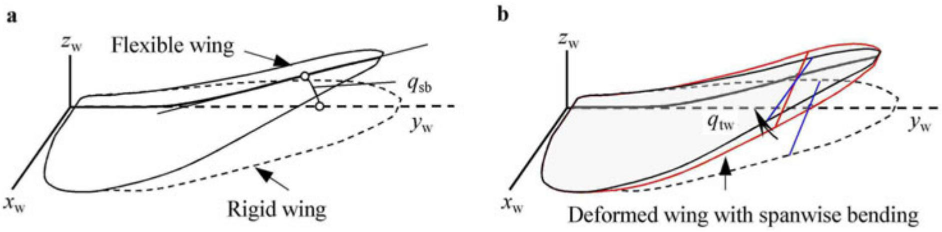

Fig. 5 Definition of **a** spanwise bending angle θ_{b} and **b** twist angle θ_{tw} in a flexible wing. Computed wing deformations are described in a wing base-fixed coordinate system

as the large aerodynamic forces as described in the preceding section. Then the wing rapidly returns to its original flat shape until a phase of 50° and eventually converges to some level around 180° after experiencing some slight fluctuations. Corresponding to the time courses of aerodynamic forces in Figs. 4a and 4b the twist and spanwise bending also demonstrates a pronounced decrease during the interval from 360° to 720°. Note that at higher angles of attack slight fluctuations in twist and spanwise bending are observed after 540°, which are induced by the unstable vertical and horizontal forces as shown in Figs. 4a and 4b.

3.3 Aerodynamic performance during unsteady phase

Figure 6 shows the time-averaged vertical force coefficients C_v, horizontal force coefficients C_h, and their ratios $C_\mathrm{v}/C_\mathrm{h}$ versus angles of attack. Note that these time-averaged value were calculated by using each time-varying value in the two-interval (unsteady and steady phases) as shown the shaded areas in Fig. 4. Table 1 further gives those values at four angles of attack. During the unsteady phase when the wing rotates from 0° up to 180°, the vertical force coefficient increases with increasing angle of attack till the AoA of 40° but then shows a drop at the AoA of 60°. The horizontal force coefficient, however, shows a monotonic increase at four angles of attack. Such correlation between the time-averaged force and angle of attack is also observed by Usherwood and Ellington [7] and by Dickinson et al. [10]. Note that this tendency is also seen here in the case of the flexible wing. We further compare the discrepancy between rigid and flexible wings. Interestingly, we see that the FSI-based wing deformations lead to a reduction of horizontal force coefficients at all four angles of attack as shown in Fig. 6a and in Table 1. The vertical force coefficients (Fig. 6b), however, show a divergent result: the flexible wing underperforms the rigid wing at lower angles of attack of 10°–20°, but outperforms the rigid wing at higher angles of attack of 40°–60° Furthermore, the vertical-to-horizontal force ratio $C_\mathrm{v}/C_\mathrm{h}$ of the flexible wing outperforms the rigid wing at all four angles of attack (Fig. 6c). Our results demonstrate that the flexible wing undergoing revolving is capable to achieve better aerodynamic performance during the unsteady (acceleration) phase. Moreover, it is interesting to find that the vertical-to-horizontal force ratio shows a pronounced increase with increasing the angle of attack with a net increase of 9.3%, 12.7%, 14.0%, 15.0% compared with that of the rigid wing at the angle of attack of 10°, 20°, 40°, 60°, respectively.

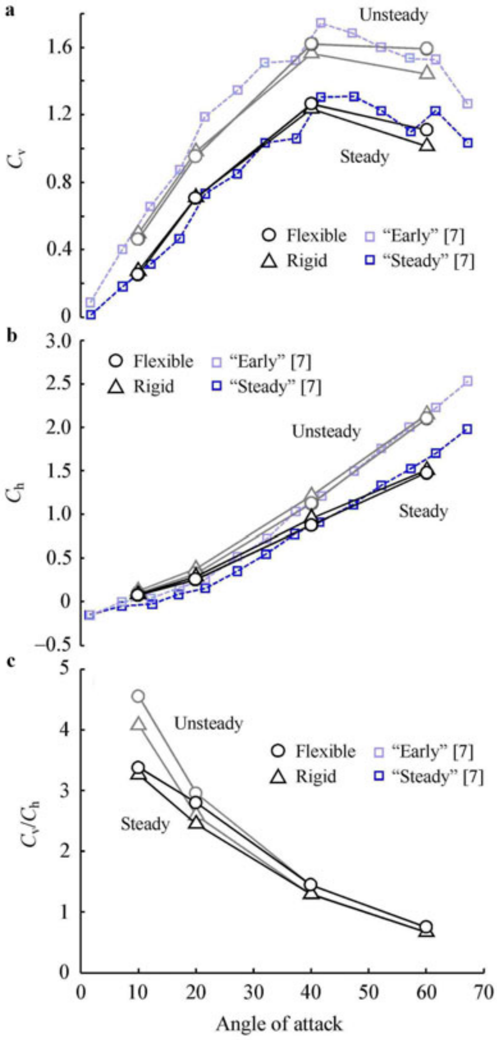

Fig. 6 Effects of angle of attack on **a** vertical and **b** horizontal force coefficients, and **c** vertical to horizontal force coefficient ratio in revolving flexible and rigid wings. Experimental results by Usherwood and Ellington [7] are also plotted for comparison

Table 1 Force coefficients during unsteady phase at four angles of attack

Angle of	C_v		C_h		$C_\mathrm{v}/C_\mathrm{h}$	
attack/(°)	Flexible	Rigid	Flexible	Rigid	Flexible	Rigid
10	0.46	0.50	0.10	0.12	4.46	4.08
20	0.95	0.98	0.32	0.38	2.93	2.60
40	1.62	1.56	1.12	1.22	1.47	1.29
60	1.59	1.44	2.10	2.15	0.77	0.67

Here we further take one case at angle of attack of 40° for instance to give an extensive discussion on aerodynamic performance during unsteady (acceleration) phase. Note that this angle of attack corresponds to the cycle-averaged feathering angle of a flapping wing in hawkmoth hovering, and the corresponding aerodynamic performance of the flexible revolving wing obtained here can be used to predict and analyze that of the flexible flapping hawkmoth wing. As shown in Figs. 7a and 7b the maximum vertical and horizontal force coefficients produced by the flexible wing are at least 25% larger than those of the rigid wing and the timing is obviously largely delayed. Such delayed timing of the maximum aerodynamic forces in the flexible revolving wing actually corresponds with a delayed LEV very similar with that observed in a flapping flexible wing by Nakata and Liu [3]. As illustrated in Figs. 8 and 9 the visualized pressures and spanwise vorticity on upper wing surface completely support such delayed LEV mechanism of the flexible revolving wing model. The pressure contours on upper surfaces of flexible and rigid wings show significant discrepancy as well as the spanwise vorticity does at $0.5R$ and $0.8R$. Note that the flow visualizations are done at three points of A, B, and C (Fig. 7) corresponding to three phase angles of wing revolution of 23.74°, 31.06°, and 38.27°, respectively. In addition, as can be seen in Figs. 7c and 7d and Figs. 9a–9c, the twist and spanwise bending in the flexible wing result in some pitch-up rotation at wing tip, which is likely capable to stabilize the LEVs and hence to enhance the generation of both vertical and horizontal forces.

3.4 Aerodynamic performance during steady phase

During the steady phase when the wing rotates from 720° up to 1 080° as shown in Fig. 6 and Table 2 the plots of force coefficient against angle of attack show similar tendency with that of the unsteady phase; the flexible wing outperforms the rigid wing at higher angles of attack of 40°–60° and is capable to achieve better aerodynamic performance. Here the vertical-to-horizontal force ratio also shows a pronounced increase with increasing the angle of attack with a net increase

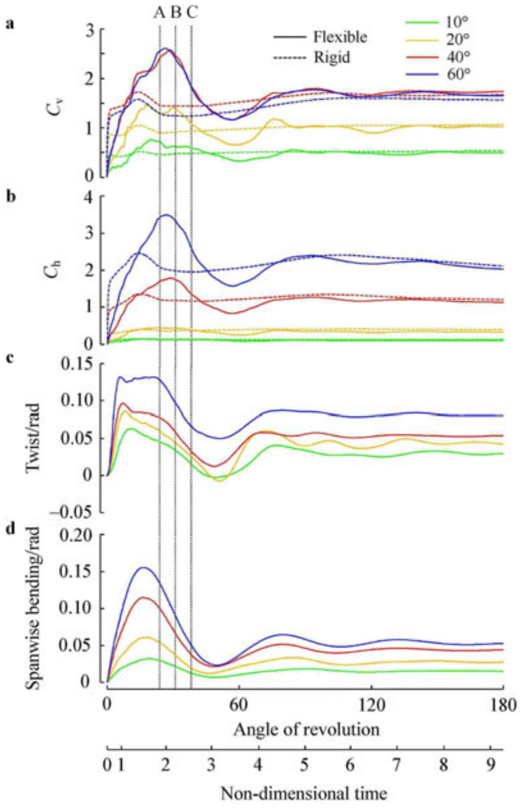

Fig. 7 Time courses of **a** vertical and **b** horizontal force coefficients of revolving flexible and rigid wings, and **c** twist, **d** spanwise bending of a flexible revolving wing during unsteady phase

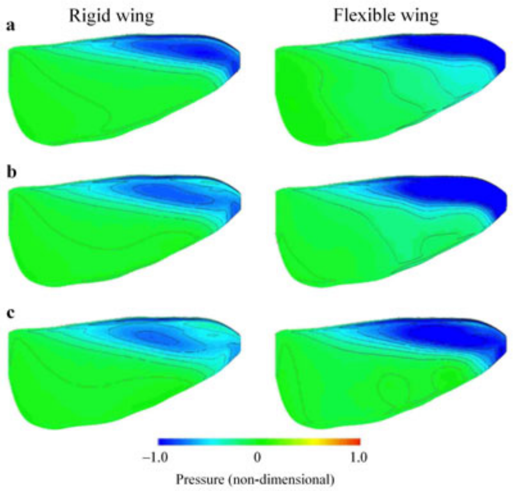

Fig. 8 Pressure contours on upper surfaces of flexible and rigid wings at instants A–C in Fig. 7

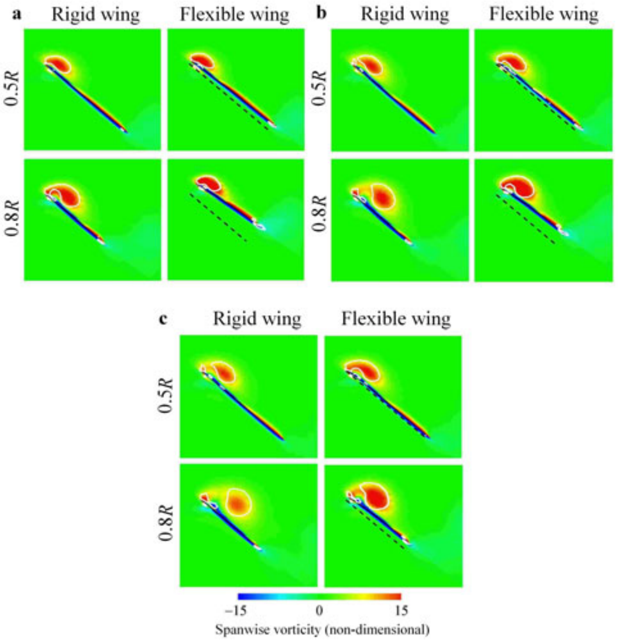

Fig. 9 Spanwise vorticity around rigid and flexible wings at instants A–C (Fig. 7) with AoA of 40°. Cross-section of a rigid wing is superimposed in the results of flexible wing by dotted line for comparison. White solid lines represent contours of constant Q criterion

Table 2 Force coefficients during steady phase at four angles of attack

Angle of attack/(°)	C_v		C_h		C_v/C_h	
	Flexible	Rigid	Flexible	Rigid	Flexible	Rigid
10	0.26	0.28	0.075	0.08	3.38	3.28
20	0.71	0.71	0.25	0.29	2.80	2.45
40	1.27	1.24	0.88	0.96	1.45	1.30
60	1.11	1.01	1.48	1.51	0.75	0.68

of 3.0%, 14.3%, 11.5%, 10.3% compared with that of the rigid wing at the angle of attack of 10°, 20°, 40°, 60°, respectively.

Note that the time-varying force coefficients and wing deformations, at higher angles of attack of 40°–60°, show comparatively large fluctuations in both flexible and rigid wings (Figs. 4a and 4b). Such fluctuating feature observed in the aerodynamic forces is probably caused by the breakdown and shedding of LEVs and tip vortices, which may result in some unstable vortex structures at wing tip. Liu et al. [24] pointed out that the tip vortex generates some reverse pressure gradient on the wing surface and hence creates a reverse axial flow in the half of the down-stroke; Harbig et al. [11] reported that as Reynolds number increases, the LEV tends to evaluate to two co-rotating vortex structures with a smaller counter-rotating vortex created as well as some adverse pressure gradient through the core of the vortex.

Again with consideration of the case at angle of attack of 40° in order to give an extensive discussion on aerodynamic performance during the steady phase, we find that the vertical force coefficient of the flexible wing is slightly higher than that of the rigid wing but the horizontal force coefficient is approximately 10% lower. Furthermore, it is seen that the slight fluctuations in twist and spanwise bending are less than 1.0°, which should have less influence on the flow structures. These are supported as shown in Figs. 10 and 11 by the visualized pressure contours and spanwise vorticity of flexible and rigid wings at three angles of wing revolution of 802°, 904°, and 997°, in which the discrepancy between flexible and rigid wings is margin. Figure 12 shows time courses of local angle of attack of the flexible wing from wing base to wing tip at AoA of 40°. At positions of $0.2R$ and $0.4R$, the local angle of attack is reduced merely less than 1.0°, but when the position is greater than $0.4R$ the angle of attack shows a reduction by 2.0° to 5.0°.

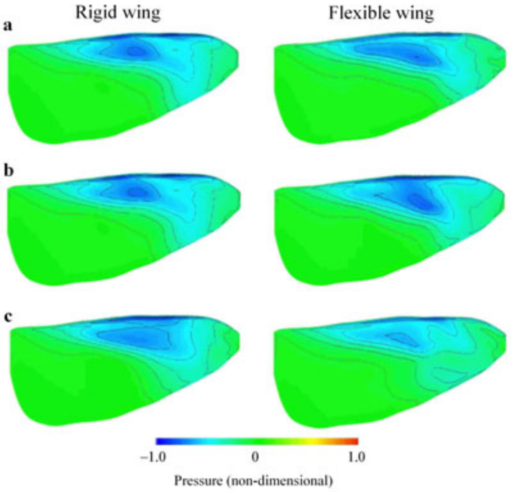

Fig. 10 Pressure contours on upper surfaces of flexible and rigid wings at angle of wing revolution of **a** 802°; **b** 904°, and **c** 997°

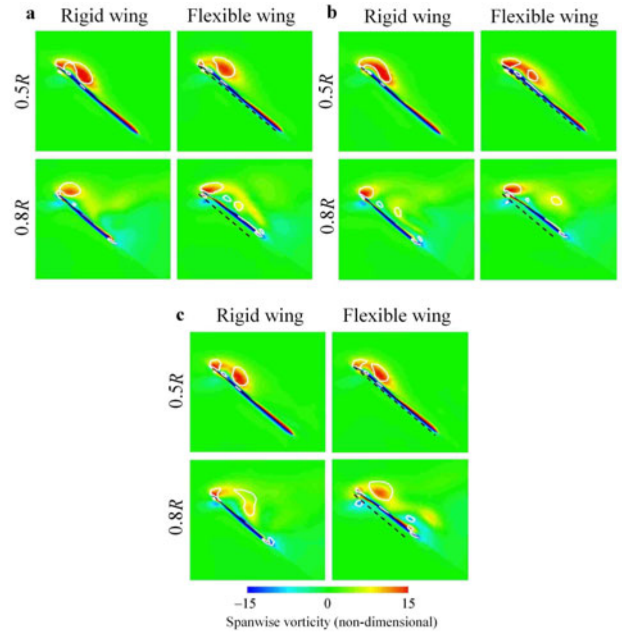

Fig. 11 Spanwise vorticity around rigid and flexible wings at angle of wing revolution of **a** 802°; **b** 904°, and **c** 997° with AoA of 40°. Cross-section of a rigid wing is superimposed in the results of flexible wing by dotted line for comparison. White solid lines represent contours of constant Q criterion

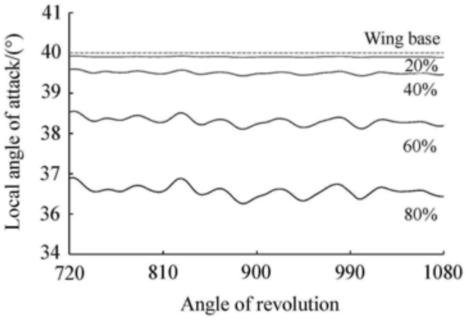

Fig. 12 Time courses of local angles of attack of a flexible wing from wing base to tip during steady phase at AoA of 40°

4 Conclusions

In this study, the effects of wing deformation on aerodynamic performance of a revolving insect wing model are investigated by using a hawkmoth wing model and FSI-based simulations. It is confirmed that the wing flexibility can enhance the aerodynamic performance of the flexible revolving wing both during acceleration (an unsteady phase) that replicates the flapping wing kinematics of a hovering hawkmoth and during steady rotation (a steady phase) particularly when the angle of attack is large sufficient to match the mean feathering angle of a hovering hawkmoth. The flexible wing model can generate much greater aerodynamic forces than the rigid wing does during the acceleration phase because the dynamic wing deformations owing to the wing acceleration that results in large inertial and aerodynamic forces can reduce the angle of attack at wing tip. During the phase of steady rotation, the wing deformation is comparatively smaller but the wing twist can still reduce the angle of attack at wing tip and hence increases the vertical force at higher angles of attack (40°–60°) while reducing the horizontal force. Both of these (acceleration-based) unsteady and steady (rotation) mechanisms for the flexible revolving wing model presumably hold more or less for flexible flapping wings as well. Moreover, our results demonstrate that the fluid-structure interaction is important and essential in evaluating the aerodynamic performance of flexible flapping wings and even in the simplified case of the revolving wing model, the wing deformation due to inertial force/aerodynamic force can enhance the aerodynamic performances but in different manner during acceleration/steady rotation.

Acknowledgement The project was partly supported by the Grant-in-Aid for Scientific Research (21360078 and 18100002) and Grant-in-Aid for Scientific Research on Innovative Areas (24120007, JSPS).

References

1 Du, G., Sun, M.: Effects of wing deformation on aerodynamic forces in hovering hoverflies. J. Exp. Biol. **213**, 2273–2283 (2010)

2 Mountcastle, A.M., Combes, S.A.: Wing flexibility enhances load-lifting capacity in bumblebees. Proc. R. Soc. B **280**, 20130531 (2013)

3 Nakata, T., Liu, H.: Aerodynamic performance of a hovering hawkmoth with flexible wings: A computational approach. Proc. R. Soc. B **279**, 722–731 (2012)

4 Tanaka, H., Whitney, J.P., Wood, R.J.: Effect of flexural and torsional wing flexibility on lift generation in hoverfly flight. Integr. Comp. Biol. **51**, 142–150 (2011)

5 Young, J., Walker, S.M., Bomphrey, R.J., et al.: Details of insect wing design and deformation enhance aerodynamic function and flight efficiency. Science **325**, 1549–1552 (2009)

6 Zheng, L., Hedrick, T.L., Mittal, R.: Time-varying wing-twist improves aerodynamic efficiency of forward flight in butterflies. PLoS ONE **8**, e53060 (2013)

7 Usherwood, J.R., Ellington, C.P.: The aerodynamics of revolving wings. I. Model hawkmoth wings. J. Exp. Biol. **205**, 1547–1564 (2002)

8 Usherwood, J.R., Ellington, C.P.: The aerodynamics of revolving wings. II. Propeller force coefficient from mayfly to quail. J. Exp. Biol. **205**, 1565–1576 (2002)

9 Lentink, D., Dickinson, M.H.: Rotational accelerations stabilize leading edge vortices on revolving fly wings. J. Exp. Biol. **212**, 2705–2719 (2009)

10 Dickinson, M.H., Lehmann, F.O., Sane, S.P.: Wing rotation and the aerodynamic basis of insect flight. Science **284**, 1954–1960 (1999)

11 Harbig, R.R., Sheridan, J., Thompson, M.C.: Reynolds number and aspect ratio effects on the leading-edge vortex for rotating insect wing planforms. J. Fluid Mech. **717**, 166–192 (2013)

12 Harbig, R.R., Sheridan, J., Thompson, M.C.: Relationship between aerodynamic forces, flow structures and wing camber for rotating insect wing planforms. J. Fluid Mech. **730**, 52–75 (2013)

13 Zheng, L., Hedrick, T., Mittal, R.: A comparative study of the hovering efficiency of flapping and revolving wings. Bioinspir. Biomim. **8**, 036001 (2013)

14 Aono, H., Liu, H.: Vortical structure and aerodynamics of hawkmoth hovering. J. Biomech. Sci. Eng. **1**, 234–245 (2006)

15 Combes, S.A., Daniel, T.L.: Into thin air: contributions of aerodynamic and inertial-elastic forces to wing bending in the hawkmoth Manduca sexta. J. Exp. Bio. **206**, 2999–3006 (2003)

16 Willmott, A. P., Ellington, C.P.: The mechanism of flight in the hawkmoth Manduca sexta. I. Kinematics of hovering and forward flight. J. Exp. Bio. **200**, 2705–2722 (1997)

17 Nakata, T., Liu, H.: A fluid-structure interaction model of insect flight with flexible wings. J. Comput. Phys. **231**, 1822–1847 (2012)

18 Liu, H., Kawachi, K.: A numerical study of insect flight. J. Comput. Phys. **146**, 124–156 (1998)

19 Liu, H.: Integrated modeling of insect flight: From morphology, kinematics to aerodynamics. J. Comput. Phys. **228**, 439–459 (2009)

20 Ellington, C.P.: The aerodynamics of hovering insect flight. II. Morphological parameters. Phil. Trans. R. Soc. Lond. B **305**, 17–40 (1984)

21 Ertas, A., Krafcik, J.T., Ekwaro-Osire, S.: Performance of an anisotropic Allman/DKT 3-node thin triangular flat shell element. Compos. Eng. **2**, 269–280 (1992)

22 Bathe, K.J., Ramm, E., Wilson, E.L.: Finite element formulation for large deformation dynamic analysis. Int. J. Numer. Meth. Eng. **9**, 353–386 (1975)

23 Mohan, P., Kapania, R.K.: Updated Lagrangian formulation of a flat triangular element for thin laminated shells. AIAA J. **36**, 273–281 (1998)

24 Liu, H., Ellington, C.P., Kawachi, K., et al.: A computational fluid dynamic study of hawkmoth hovering. J. Exp. Biol. **201**, 461–477 (1998).